Article

High-Frequency Modelling of Electrical Machines for EMC Analysis

Yerai Moreno [1,*], Aritz Egea [1], Gaizka Almandoz [1], Gaizka Ugalde [1], Ander Urdangarin [2] and Roberto Moreno [3]

1   Faculty of Engineering, Mondragon Unibertsitatea, 20500 Mondragón, Spain; aegea@mondragon.edu (A.E.); galmandoz@mondragon.edu (G.A.); gugalde@mondragon.edu (G.U.)
2   ORONA Elevator Innovation Centre, 20120 Hernani, Spain; aurdangarinl@orona-group.com
3   IKERLAN, 20500 Mondragón, Spain; rmoreno@ikerlan.es
*   Correspondence: ymoreno@mondragon.edu

Abstract: The trend towards electrification in mobility has led to the increased use of silicon carbide (SiC) semiconductors. These semiconductors are more efficient but also present challenges related to electromagnetic interference (EMI) due to their higher voltage derivatives. This paper introduces a new high-frequency impedance model for electrical machines. The proposed model distinguishes itself from existing approaches by being entirely derived from Finite Element Method (FEM) simulations, which include capacitances in the magnetic simulation. This approach achieves a balance between computational efficiency and high accuracy across the entire frequency spectrum, ranging from 100 Hz to 50 MHz. The model provides valuable insights during the design phase and was rigorously validated using data from 28 samples of an industrial machine.

Keywords: computer simulation; electric machines; electromagnetic compatibility; finite element methods; high frequency

1. Introduction

In the context of electrifying mobility, improving the efficiency of electrical drives to reduce pollution and decrease energy consumption is essential. The analysis in [1] showed that silicon carbide (SiC) devices can contribute to this objective by improving power density, dynamic response, and energy efficiency. Their high working frequency and low switching losses enable more compact inverter and motor designs with higher efficiency.

However, working with Wide-Band-Gap (WBG) switches at higher frequencies may cause serious electromagnetic interference (EMI) problems due to their high voltage derivatives, which could also affect the robustness of electrical machines. Converters supply electrical machines with frequency- and amplitude-modulated voltages, which can generate large voltage derivatives. As the frequency increases, these derivatives also increase, resulting in higher overvoltages at the motor terminals. This can deteriorate the insulation of the winding and even cause protection failures in the event of a short circuit or contact defects [2,3].

Additionally, modulated voltages can generate a common-mode voltage (CMV). The CMV is converted into a current that flows to the ground, which could damage the drive's components. For example, the voltage induced in the shaft can cause bearing currents, leading to their deterioration. Additionally, it can affect other elements connected to the same network, such as sensors and safety systems in electric vehicles [4]. This phenomenon is referred to as conducted EMI and is usually analysed in the range of 150 kHz to 30 MHz.

Several solutions have been proposed to reduce the effects of undesired CMV in the shaft and bearings. These include using insulated or ceramic bearings; applying different

conductive greases; and adding Faraday shielding, brushes, or shaft grounding rings [5,6]. However, these solutions only address the CMV effects on the bearings.

To reduce electromagnetic interference (EMI) throughout the entire electrical machine, shielded cables are recommended, along with grounding, to provide a low-impedance path for the CMV. Various inverters and modulation techniques have been proposed to reduce the generation of CMV from the source [5,7,8]. However, the most commonly used technique to prevent electromagnetic interference (EMI) from entering the grid is to add a filter to the drive [9].

Most solutions involve adding components to the drive, which increases its cost, volume, and weight, as well as the complexity of the system. Furthermore, add-ons are typically included only after EMC tests have failed and corrective action is required to comply with regulations and bring the product to market.

Therefore, an EMI strategy-based design should be implemented early in the development cycle to decrease product development costs, enhance reliability, and achieve the optimal solution. As a result, comprehending and predicting EMI noise using high-frequency models during the design stage is crucial to effectively manage this noise on the device level.

Most models proposed in the literature are empirical, with parameters calculated using analytical approximations from measurements or fitting procedures [10–16]. These models are generally more accurate and quicker to develop but require experimental prototypes for calibration. However, the design of electrical machines from the EMC perspective must be considered in the early stages of the design process, when prototyping is usually still not an option. Therefore, developing such a model using other means, such as Finite Element Method (FEM) simulations, before manufacturing is essential.

FEM machine models have previously been proposed for the design stage [17–26]. These models are mainly based on 2D FEM simulations, which model all the strands of the coils but require high computational capabilities and long simulation durations. Regarding the frequency range, most machine models do not exceed 10 MHz, or, even if they do (e.g., [17,27]), they may not provide accurate results throughout the entire range. Furthermore, the damping effect at the resonance point, caused by the behaviour of the ferromagnetic core at high frequencies, is frequently underestimated. For more details, refer to the comprehensive review of high-frequency analysis and modelling tools for electrical machines conducted in [28].

Two simulations are generally conducted: an electrostatic simulation to obtain the capacitance values in the equivalent model and a magnetic simulation to determine the inductance and resistance values. The resulting RLC values are then introduced into a circuit simulation tool, and the impedances are calculated. However, this approach causes the current that would flow through the capacitors to instead flow through the resistance and inductance in the magnetic simulations, resulting in different RL values. The inductance values may change at high frequencies as a result of capacitive couplings that cause the current paths to change.

In this paper, these capacitive couplings are considered during magnetodynamic FEM simulations to accurately compute the inductance values.

This paper presents a high-accuracy and low-computational-load simulation approach for calculating the high-frequency (100 Hz to 50 MHz) impedance of electrical machines. The novelty compared with other models is that the impedances, including the capacitances in the magnetic simulation, are calculated entirely via FEM simulations with a fast and accurate model.

In addition, while the models in the literature were mostly validated by measuring the impedance of one or two machines, in this study, the impedance of 28 industrial machines was used for validation. Thus, we could consider the influence of manufacturing tolerances on the impedance value.

This is a continuation of previous work in which high-frequency phenomena were analysed in detail using small and controlled coil models [29].

The structure of the paper is as follows. The methodology for modelling a high-frequency electrical machine is described in Section 2. Both electrostatic and magnetodynamic simulations are described in this section, with full and simplified definitions.

Then, a step-by-step validation of the model is presented in Section 3, starting with one coil of the machine and proceeding to two coils, one phase, and finally the whole machine. The difference between the full definition and the simplified model is also analysed in Section 3. Section 4 discusses the results in detail. Finally, in section Section 5, the main conclusions are outlined, and the future challenges for an effective EMC-oriented design are highlighted.

2. Methodology

This section presents a methodology that improves upon the methodology presented in [29]. As the parasitic capacitances change the current distribution in the windings, they are calculated initially with an electrostatic FEM simulation. Then, these capacitances are included in the magnetodynamic FEM model to obtain complete and accurate values for the desired common-mode or differential-mode impedances. Altair Flux™ 2023 (Altair Engineering, Troy, MI, USA) is used for this task. The process is summarised in Figure 1. The properties of the magnetic core must be defined properly in the magnetodynamic simulation to obtain accurate results.
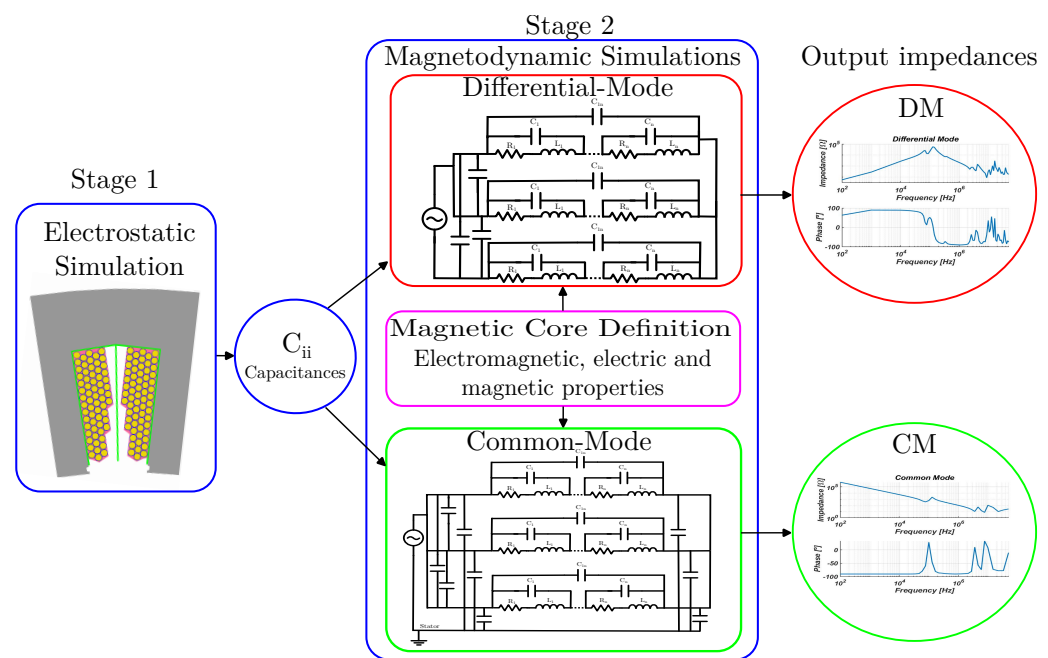

Figure 1. Simulation methodology.

2.1. Electrostatic Simulation

The capacitances between the conductors as well as the conductor to stator capacitances are calculated in the electrostatic simulation. Only one slot of the machine needs to be considered, and all the conductors in the slot are described with their insulating and impregnation materials.

The Gauss law method is used for this purpose, performing one simulation per conductor. In each simulation, all conductors are set to 0 V except one, the jth conductor, which is set to V_j V. Then, the expression (1) is applied after solving the electric field distribution, where Q_{ij} is the charge of each conductor due to the voltage excitation:

$$C_{ij} = 2\frac{Q_{ij}}{V_j} \tag{1}$$

Then, the stator is set to V_j V, and the capacitances from the conductors to the stator are obtained.

As explained in [29], an $n \times n$ matrix of capacitances is obtained from the simulation, where n is the number of conductors per slot. Another $n \times 1$ matrix that contains the conductor-to-stator capacitances is also obtained from the simulation. These capacitances are required in the magnetodynamic simulation.

As mentioned in the introduction, a full conductor-based model is presented initially that individually simulates each defined conductor of the machine. Then, by using bulk coils instead of individual conductors, a simplified model is presented. A bulk coil is a group of x conductors that behave as a single unit. This simple model reduces the complexity and computation time of the simulation. The difference between the definitions of the two models is shown in Figure 2.
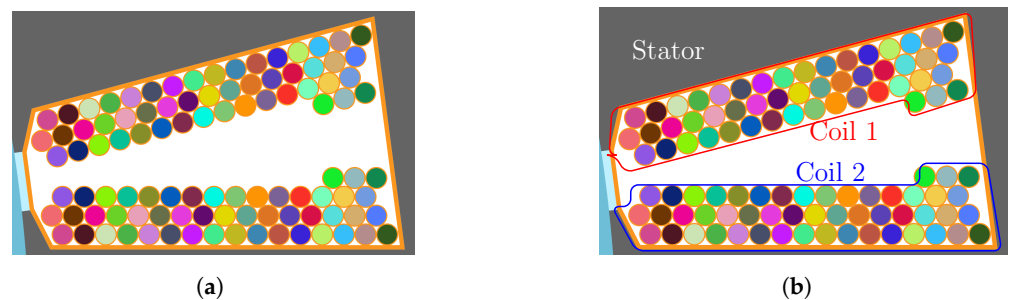

Figure 2. Electrostatic models: (**a**) full; (**b**) simplified to two bulk coils rounded in blue and red.

Taking into account the definition shown in Figure 2a, where 50 conductors per coil are defined, a capacitance matrix of 100×100 and 100 capacitive couplings to the stator are computed for the full definition model.

As Figure 2b shows, the simplified model is geometrically identical, but the conductors on either side of the slot are grouped and set to the same voltage. Thus, three objects are included in the simulation: two coil sides and the stator core. The individual conductors are still drawn to maintain as much geometrical detail as possible, even though only three nodes are defined and three capacitances are obtained: the coil side to the stator (C_{ws}), the coil capacitance (C_w), and the coupling between the coil sides in the same slot (C_{ww}).

Once the capacitive couplings are extracted in either of the definition models, a magnetodynamic simulation is conducted to obtain the common-mode (CM) and differential-mode (DM) impedances.

2.2. Magnetodynamic Simulation

The magnetic FEM model is geometrically identical to the electrostatic model. However, the former requires the correct definition of a fine mesh within the perimeter of the conductors to take into account the skin and proximity effects. Another key factor in this magnetic model is the correct definition of the magnetic core, which is explained in detail in core modelling section.

A single coil of the machine is shown in Figure 3 to compare the definitions of the detailed and simplified models.

Figure 3. Magnetodynamic models: (**a**) full; (**b**) simplified.

For the detailed model (Figure 3a), all the conductors are drawn, and the mesh is adapted to the perimeter of individual conductors depending on the frequency. However, simulating the full machine (our main objective) would mean simulating 100 conductors per slot, in a machine of 36 slots. Even applying symmetries and periodicities, the full model would require an excessive computational load due to the many capacitive couplings and the fine mesh in individual conductors.

The simulation time and computational load can be significantly reduced if the coil is simplified to a bulk coil, as shown in Figure 3b. Defining the turn number and conductor diameter and only drawing the slot perimeter, as in low-frequency models, the skin and proximity effects are taken into account by the simulation software. This avoids drawing all the conductors with a fine mesh.

Once the geometry is defined, the circuit and its connections must be linked. The equivalent circuit of one phase is shown in Figure 4.
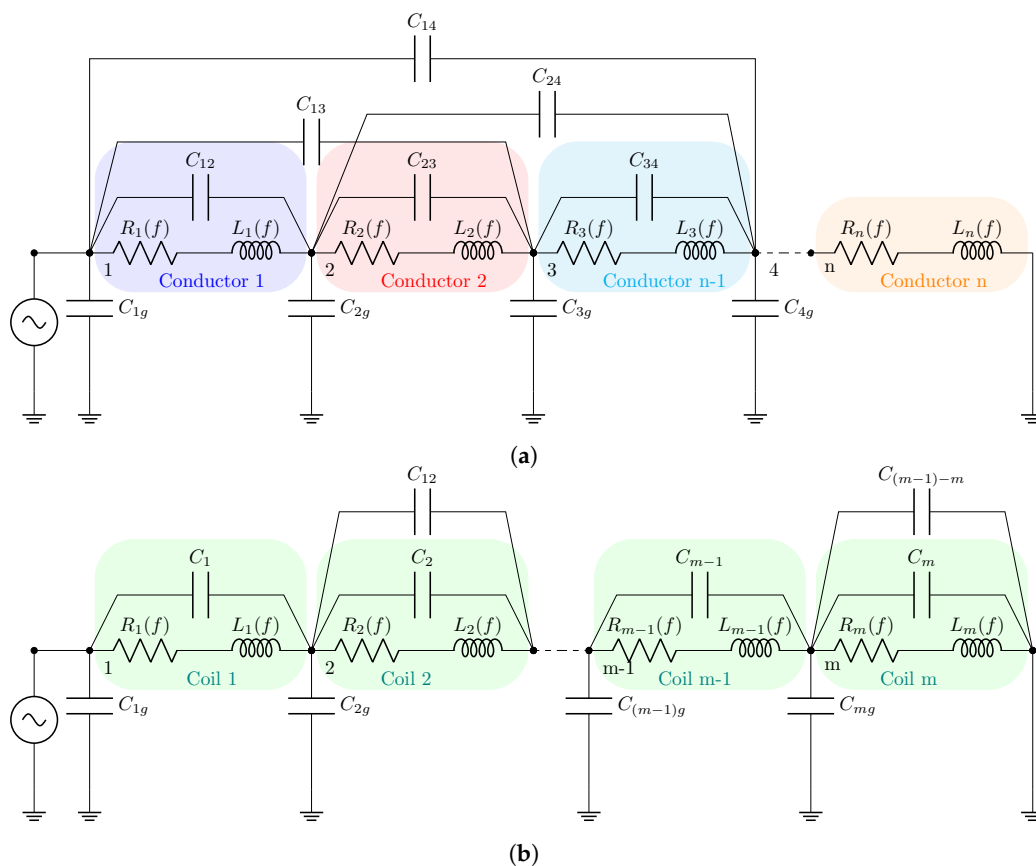

Figure 4. Per-phase equivalent circuit of an electrical machine: (**a**) full (conductor-based, each color one conductor); (**b**) simplified (coil-based).

Figure 4a shows the full definition circuit, where n is the number of conductors in one phase. Each conductor is coupled to all other conductors from the same slot via capacitances. A capacitance also exists between each conductor in the slot and the stator.

For the simplified definition circuit in Figure 4b, m is the number of coils, and capacitive couplings only exist between the coil sides (C_1), between the coils in the same slot (C_{12}), and between the coils and the stator (C_{1g}); thus, the number of couplings is considerably reduced.

The validation and comparison of the models is presented in Section 3.1, considering the impedance of one coil of the machine.

Core Modelling

Normally, when modelling an electrical machine with the FEM, the core material is defined by a constant permeability or, if more accuracy is required, by its BH curve. The iron core losses can then be post-processed using different methods [30]. The ferromagnetic cores in the machines are laminated to limit the eddy current losses in the working frequency.

However, at a high frequency, the skin depth is less than the lamination width, and the eddy currents are enhanced in the core surface. This increases the losses and creates a shielding effect that prevents the magnetic flux from penetrating the core, reducing the inductance of the coils. To model this effect in detail, a 3D FEM model would be needed to simulate a magnetic core with individual sheets [31]; however, this would require considerable computational effort.

According to the literature, a suitable method for investigating the eddy currents induced in a laminated magnetic core without considering each laminated sheet is to determine the frequency-dependent effective complex relative permeability [18,21]. This method also includes hysteresis losses.

In Figure 5, the impedance of one coil of a machine is shown. On the one hand, the BH curve simulation overestimates the impedance around the resonance point, as the shielding effect and the core eddy current losses are not taken into account. On the other hand, with the complex permeability, the impedance matches the measurement, and the resonance point is damped.
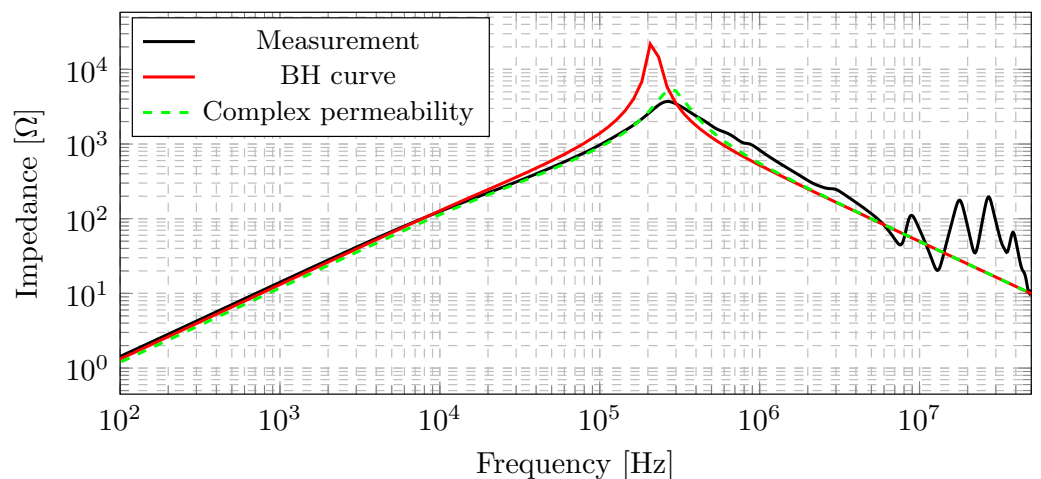

Figure 5. Influence of core modelling on the impedance of a coil.

The complex permeability model is derived from simplifying Maxwell's equations inside the laminated sheet to a one-dimensional problem. The complete development of the equations is shown in [32,33] but will be reviewed here for clarity.

Taking into account a single rectangular laminated sheet, as in Figure 6, and assuming that the current is in the y direction, the magnetic field is

$$\frac{\partial^2 H_z(\mathrm{x},t)}{\partial \mathrm{x}^2} = \frac{\partial H_z(\mathrm{x},t)}{\partial t} \tag{2}$$

Solving Equation (2) results in two waves in the opposite direction, with the propagation constant defined as $\gamma = \frac{1+j}{2\delta} = \sqrt{j\omega\mu\sigma}$, where δ is the skin depth. Assuming symmetric boundary conditions for each side of the sheet, the magnetic field inside of the sheet is

$$H_z(\mathrm{x},t) = \frac{H_0}{1 + e^{-\gamma \mathrm{w}}} \left(e^{j\omega t - \gamma(\mathrm{x}+\mathrm{w})} + e^{j\omega t - \gamma(\mathrm{x}-\mathrm{w})} \right) \tag{3}$$
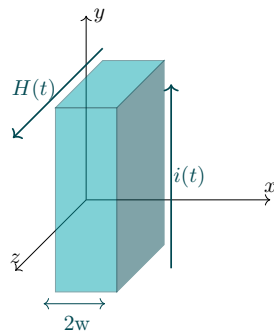
Figure 6. Single laminated sheet.

The magnetic flux can be calculated as

$$\langle B_z \rangle = \frac{1}{A_{cross}} \int_{-w}^{w} \mu H_z(x,t) \Delta y \, dx = \frac{H_0 e^{j\omega t} \mu}{\gamma} \tanh(\gamma w) \tag{4}$$

where A_{cross} is the cross-sectional area of the sheet. Then, the effective permeability μ_{eff} in the z direction of the laminated sheet can be calculated as follows:

$$\mu_{eff} = \frac{\langle B_z \rangle}{\mu_0 H_z^{ext}} = \mu_{local} \left(\mu'(f) - j\mu''(f) \right) \tag{5}$$

where H_z^{ext} is the external field, and μ_0 is the permeability of free space. The local permeability (μ_{local}) can be measured or estimated using an optimisation algorithm [33]. When measuring the impedance of the electrical machine, the injected current is low, at around 0.1 A, so the core is operating in a low-magnetisation zone.

Finally, in (6), μ' is the real part of the complex relative permeability, representing the energy storage in the core, while the imaginary part (μ'') represents the losses of the component:

$$\begin{cases} \mu'(f) & = \mu_{local} \frac{\delta}{w} \left(\frac{\sinh(w/\delta) + \sin(w/\delta)}{\cosh(w/\delta) + \cos(w/\delta)} \right) \\ \mu''(f) & = \mu_{local} \frac{\delta}{w} \left(\frac{\sinh(w/\delta) - \sin(w/\delta)}{\cosh(w/\delta) + \cos(w/\delta)} \right) \end{cases} \tag{6}$$

As the magnetic core of the analysed machine comprises M800-65A electrical sheets, the local permeability and resistivity of this material is defined using a wound toroid of M800-65A magnetic sheet, as shown in Figure 7.

Figure 7. M800-65A toroid.

The resistance and inductance of the toroidal coil are measured. From these, the complex permeability observed in Figure 8 is obtained, which agrees with the proposed complex permeability model (6).
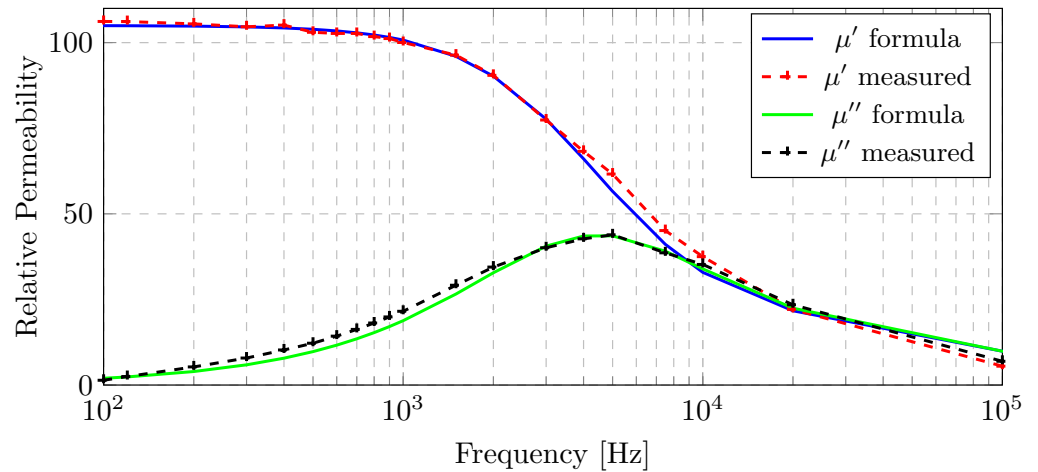
Figure 8. Complex permeability.

μ'' is zero at a low frequency, as no losses occur in the component, and it increases with the frequency. The initial value of μ' is equal to the local permeability. A low value of around 105 confirms that the core is operating at a low-magnetisation working point during the measurement. When the shielding effect appears, both permeability values decrease.

3. Modelling of an Electrical Machine—Validation

In this section, the high-frequency FEM simulation of an electrical machine is validated with experimental measurements. The main parameters of the machine are shown in Table 1.

Table 1. Parameters of analysed machine.

Stator Slots	Poles	Coils per Phase	Turns per Coil	Conductor Diameter	Core Material
36	15	12	50	1.6 mm	M800-65A

First, the two models were validated and compared with the impedance of a coil. Then, as the simplified definition model was found to be valid, a step-by-step validation was carried out using this model. We started by validating the impedance of two coils in series, followed by a full phase of the machine and, finally, the three phases of the full winding of the motor. The simulation results were compared with experimental measurements obtained using a Bode100 Impedance Analyser from Omicron (Austria).

3.1. One Coil

Common-mode (CM) and differential-mode (DM) impedance measurements of one coil were obtained as shown in Figure 9.
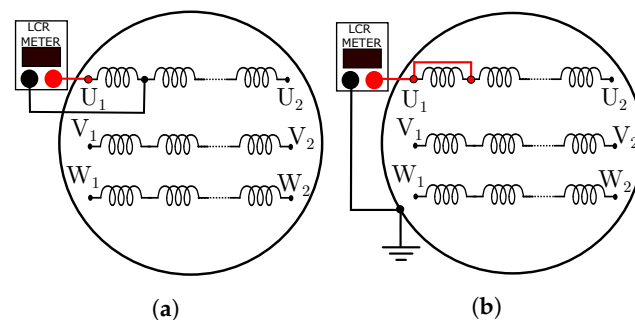

Figure 9. Experimental measurements of one coil: (**a**) DM; (**b**) CM.

Both the full and simplified models agreed with the measurements throughout the frequency range, though their accuracies differed, as shown in Figure 10. The simplified model demonstrated greater attenuation at the resonance point.

Additionally, the detailed model exhibited more resonances within the 10–30 MHz range, which were not observed in the simplified model. This discrepancy arose from the fact that the simplified model disregarded the capacitances between conductors and instead incorporated them as coil-to-coil capacitances. As a result, the intricate capacitive couplings responsible for generating these resonances were not accounted for in the simplified model. The primary resonance at 10 MHz in the common mode was attributed to the initial turns of the coils.
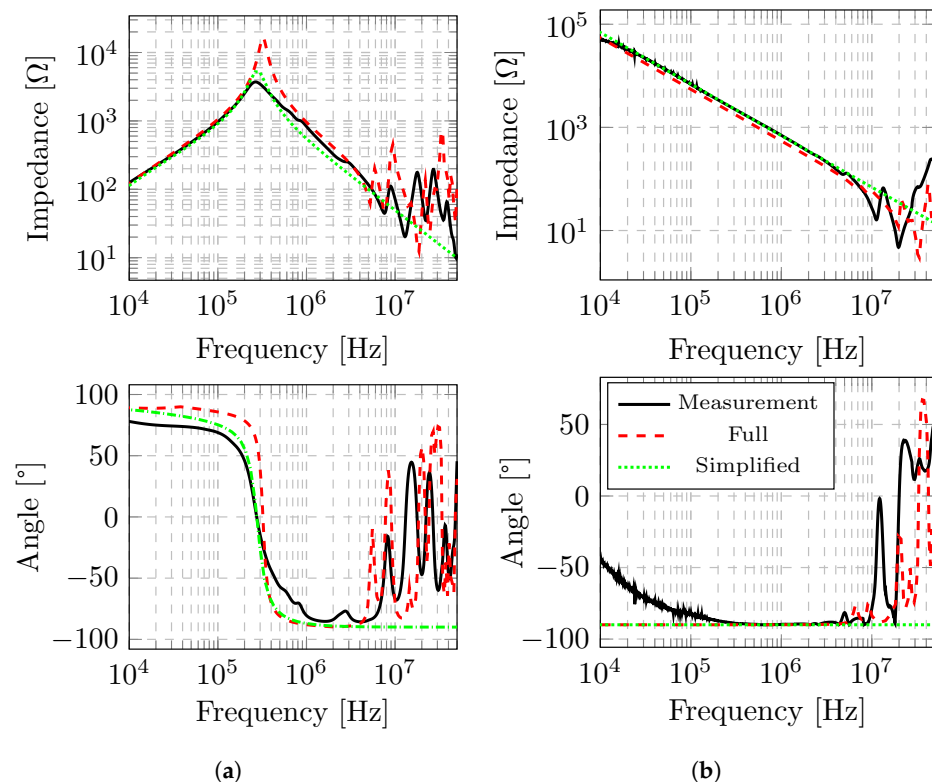
Figure 10. One coil: (**a**) differential mode; (**b**) common mode.

The simplified model displayed considerable benefits in terms of its simplicity, reduced number of parameters, and shorter simulation duration, allowing for future optimisation processes, as demonstrated by Table 2.

Table 2. Full definition vs. simplified model of a coil.

	Electrostatic FEM Simulations	Electrostatic Simulation Duration	Magnetodynamic FEM Circuit Components	Total Time for 100 Points
Full Model	51	82 min	2700	11.4 h
Simple Model	3	5 min	4	3.8 h

To obtain the matrix capacitance for a coil of 50 turns with the full definition model, 51 electrostatic simulations were needed, with a consequent increment in the number of nodes in the magnetodynamic circuit. The simple definition model reduced the simulation time by 66%.

The primary aim of this study was to create a comprehensive model of a machine. Initially, sacrificing a degree of accuracy and simulation speed by using a simplified version of the model is acceptable, as achieving a detailed definition of the full machine may

not be feasible within a reasonable time frame. Additionally, as the model is scaled up to encompass the entire machine, the impact of conductor-to-conductor capacitance in the higher frequency range will diminish, leading to improved agreement between the simulation and measurement results.

3.2. Two Coils

The next step in the validation was to measure the impedance of two coils, as shown in Figure 11, and compare it with the simulation results obtained with the simple definition model, as in Figure 12.
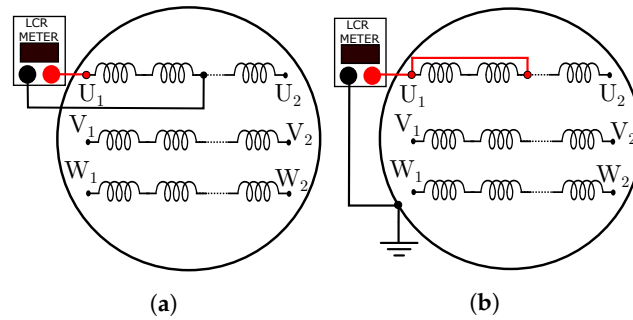

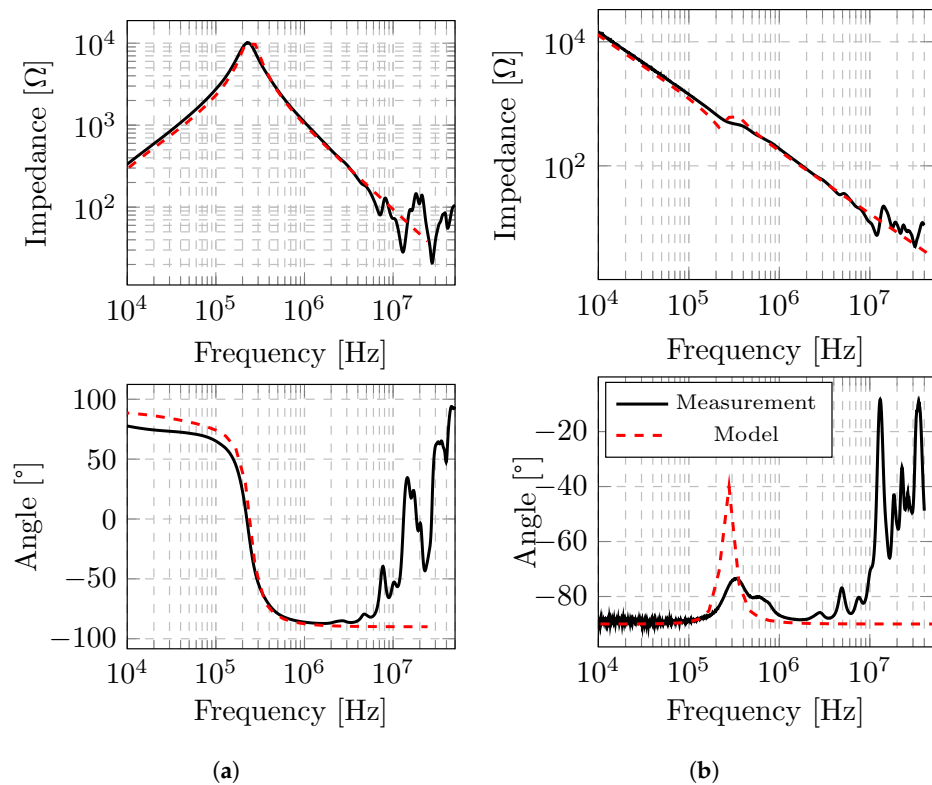**Figure 11.** Experimental measurements of two coils: (**a**) DM; (**b**) CM.

Figure 12. Two coils: (**a**) differential mode; (**b**) common mode.

The simulation results matched the measurements up to 10 MHz. In the frequency range above 10 MHz, inter-conductor capacitive couplings occurred, as with the single coil, though the number of resonances and their amplitude were lower than in the previous case. However, the overall agreement was satisfactory.

In the common-mode impedance, a resonance appeared at around 300 kHz in both the measurements and the simulation, though it was sightly under-damped in the latter case. Again, the first turns of the coils and the connection between them played a significant role in the common-mode impedance at around 10 MHz.

3.3. The Overall Phase

Once two consecutive coils were validated with close agreement up to 10 MHz, the overall phase was modelled and compared with the measurements, as shown in Figure 13.
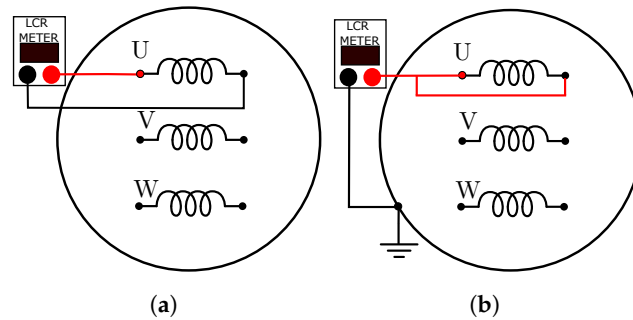

Figure 13. Overall phase: (**a**) DM; (**b**) CM.

Figure 14 shows that very close agreement between the simulation results and experimental data was achieved.
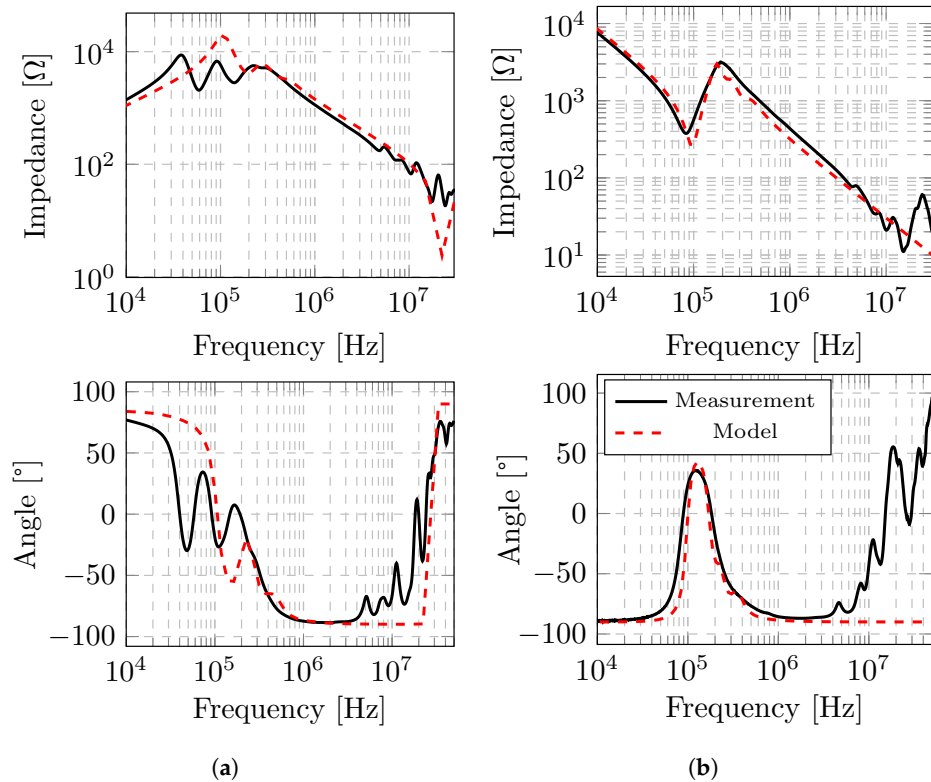

Figure 14. Overall phase validation: (**a**) DM; (**b**) CM.

Conversely, the common-mode impedance produced a more accurate result for the resonance point than in the two-coil model; the capacitive couplings between the coils in different slots may have caused disagreement about the differential-mode resonance point.

3.4. Full Machine

For the validation of the full machine model, the impedances of 28 electrical machines, including the rotor, were measured in a factory manufacturing line, as shown in Figure 15.
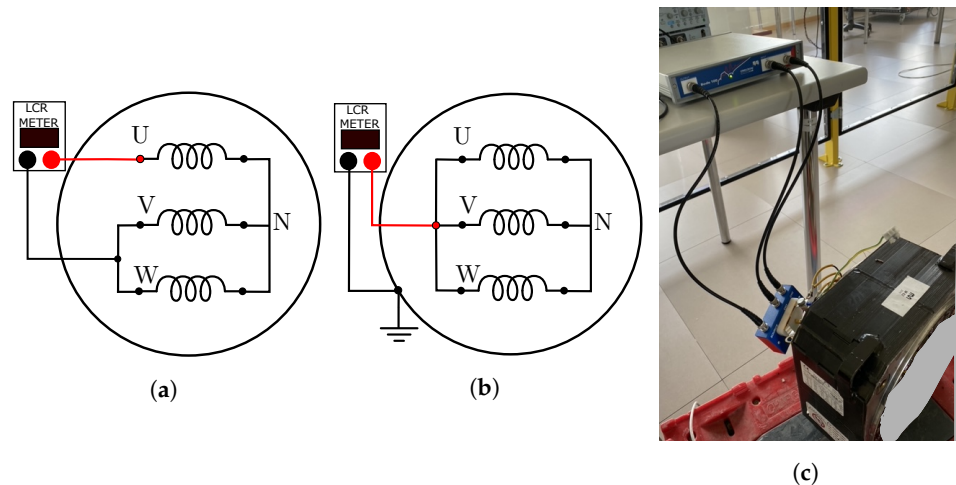
Figure 15. Experimental measurements of the machine: (**a**) DM; (**b**) CM; (**c**) experimental setup.

All the motors were of the same model, and so we assessed 28 different motors to consider the effect of the manufacturing tolerance on the measured impedance. The impedances are shown in Figures 16 and 17, where the manufacturing tolerance is indicated by the green area between the maximum and minimum measured impedances. The tolerance was very low, suggesting that the impedance of all the machines was almost equal, regardless of the manufacturing tolerance.

The measurements were carried out during the last step of the mounting line in the factory, so the rotor was included. The influence of the rotor on the high-frequency impedance is analysed later on.

Figure 16 shows that the common-mode impedance calculated via the FEM agreed closely with the experimental data across the whole frequency range.
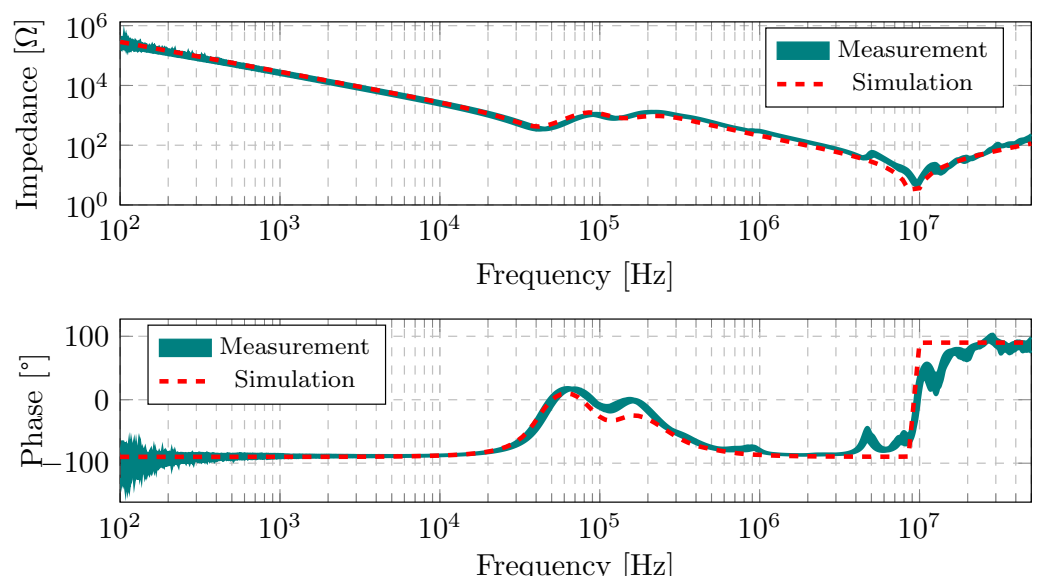

Figure 16. Simplified CM model of the machine, considering the rotor.

As in all previous impedance measurements, an inductive effect was observed around 10–20 MHz that depended on not only the measured device but also the measuring connections. Thus, an approximate measurement was conducted with different calibrations of the impedance meter, revealing that the measuring connections introduced an inductance of approximately 3.75 µH to the measured impedance. Consequently, an inductance of this value was added in series to the circuit of Figure 4.

In the differential mode, two phase connection configurations, $uv - w$ and $uw - v$, were tested in the 28 machines, and the same tolerance area was generated from the 56 measurements, as shown in Figure 17.
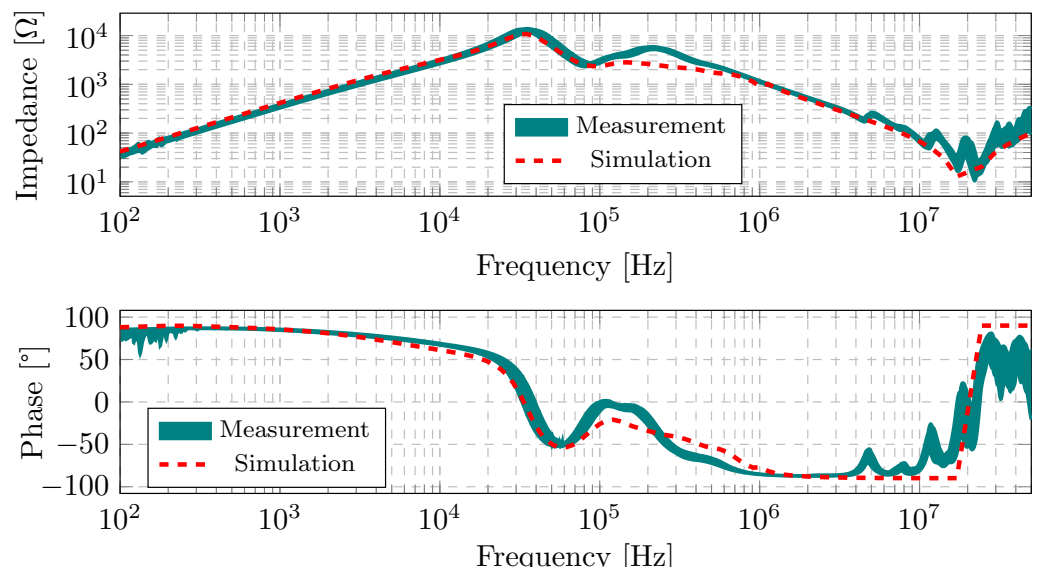

Figure 17. Machine DM simplified model, considering the rotor.

As with the common-mode impedance, the differential-mode impedance calculated via the FEM matched the experimental data (see Figure 17). As explained in the core modelling section, the complex permeability is a simplification of the core behaviour at a high frequency, and so it suffers some limitations that may have caused discrepancies in the impedance value for the resonance at 200 kHz.

Moreover, the applied model was simplified for a faster and more efficient simulation, and so the capacitive couplings between conductors were included within the coil-to-coil couplings, reducing the agreement at small resonances from 10 to 50 MHz. However, the overall accuracy obtained in this range was sufficient for the primary objective of the model, which was to predict EMI noise using high-frequency models of the drive elements (in this case, the machine).

3.5. Rotor Influence

Rotors are known to affect the impedance of electrical machines. Figure 18 shows that the presence of the rotor dampened the resonance point in the common-mode impedance.
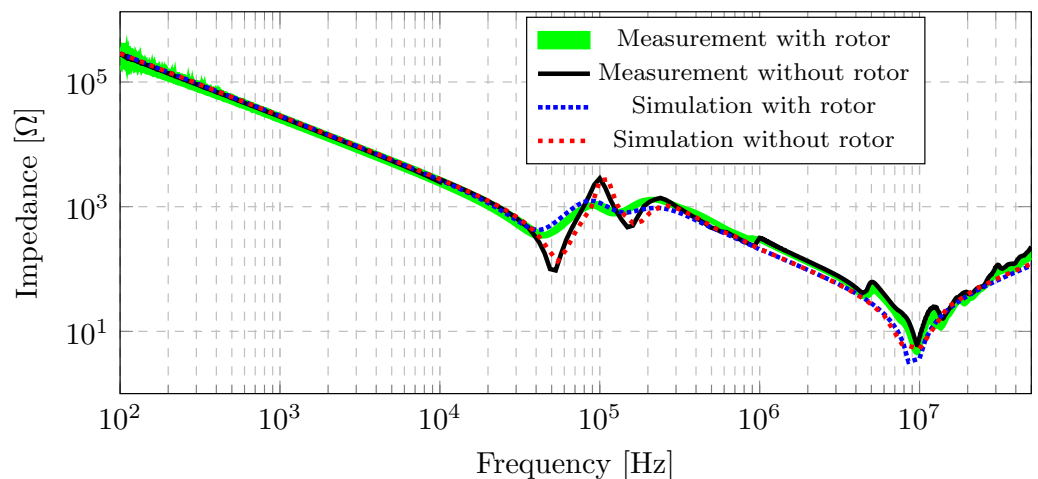

Figure 18. Rotor influence on CM impedance.

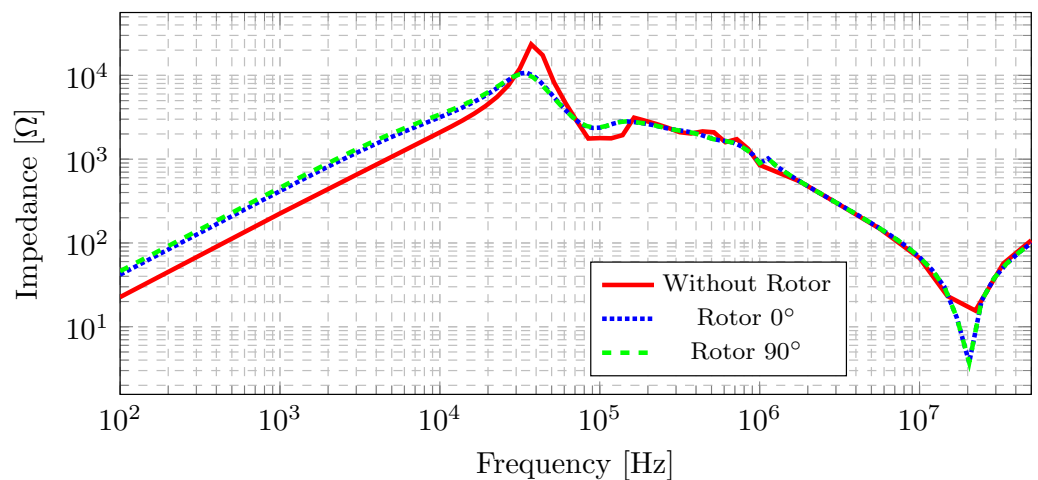The rotor also damped the main resonance in the impedance of the differential mode, as shown in Figure 19.

Figure 19. Rotor influence in DM; simulation results.

Moreover, rotor position also influences the impedance at a low frequency due to the direct and quadrature axes, but this effect does not occur in the EMC range of 150 kHz to 30 MHz, so it was disregarded by our model.

4. Discussion

This section provides a summary of the results, highlighting the most significant findings.

Firstly, we validated the modelling of the magnetic core via the complex permeability and measurements of an M800-65A laminated toroid.

Then, we compared two definition models, a detailed (or full) model and a simplified model. The impedances obtained were compared and validated with measurements. Both models showed close overall agreement. However, the simplified model did not exhibit any resonance in the 10 to 30 MHz range. This discrepancy was due to the simplified model neglecting capacitances between conductors and instead incorporating them into the coil-to-coil capacitances. However, evaluating the trade-off between accuracy and simulation time is important. In most cases, a 66% reduction in simulation time with the simplified model may be sufficient.

As the model was scaled up to the full machine, the accuracy improved due to the decreased impact of conductor-to-conductor capacitance, resulting in closer agreement between the simulation and measurement results.

Finally, we analysed the influence of the rotor by comparing the impedances in its absence and presence. We also analysed the impact of different rotor positions. The simulations and measurements showed that the presence of the rotor dampened the main resonance in the common-mode impedance. We also observed that the presence and position of the rotor affected the differential-mode impedance in the low-frequency range.

The proposed model adheres to the conventional academic structure and could be useful for future research in the EMC area. An important step will be to analyse the design and manufacturing variables that affect the high-frequency impedances of machines. This will help improve machines in terms of EMC issues, as well as enhancing their reliability.

5. Conclusions

Modelling electrical machines at a high frequency is a complex task due to the convergence of various physical phenomena. To accurately consider all these phenomena, multi-physics simulations are required, which generally lead to a significant computational load. In this study, we proposed and validated a detailed conductor model. However, to

reduce the computational load, a simpler model was developed for analysing the high-frequency behaviour of the machine. The validated model for the full machine was simpler and required a lower computational load. It was based on coils instead of conductors and was tested in terms of manufacturing tolerances. The impedances of 28 industrial machines in the range of 100 Hz to 50 MHz were measured to cover all the spectra required by the EMC standards. Both the DM and CM simulations showed high accuracy at principal resonances.

The calculation duration of the analysed machine was 66% shorter due to the simplified coil definition, which considered the capacitive coupling between coils in the same slot.

This model could be used to evaluate the design and manufacturing variables that affect the high-frequency impedances of machines. This could improve machines in terms of EMC issues and increase their reliability.

Author Contributions: Conceptualization, Y.M., G.A., A.E., G.U., A.U., and R.M.; software, Y.M. and A.E.; validation, Y.M., G.A., and A.E.; formal analysis, Y.M., G.A., and A.E.; project administration, G.A., A.U., and R.M.; supervision, G.A. and A.E.; writing—original draft, Y.M.; writing—review and editing, Y.M., G.A., A.E., G.U., A.U., and R.M. All authors have read and agreed to the published version of the manuscript.

Data Availability Statement: Data are contained within the article.

Conflicts of Interest: The authors declare no conflicts of interest.

References

1. Morya, A.K.; Gardner, M.C.; Anvari, B.; Liu, L.; Yepes, A.G.; Doval-Gandoy, J.; Toliyat, H.A. Wide Bandgap Devices in AC Electric Drives: Opportunities and Challenges. *IEEE Trans. Transp. Electrif.* **2019**, *5*, 3–20. [CrossRef]
2. Mazurck, P.; Michalski, A.; Swiatck, H.; Mazzetti, C.; Flisowski, Z. Hazard for insulation and relevant emc problems due to voltages in circuits of motor supply by pwm converters. In Proceedings of the 2003 IEEE Bologna Power Tech Conference Proceedings, Bologna, Italy, 23–26 June 2003; IEEE: Piscataway, NJ, USA, 2003; Volume 2, pp. 728–732. [CrossRef]
3. Shen, Z.; Jiang, D.; Zou, T.; Qu, R. Dual-Segment Three-Phase PMSM with Dual Inverters for Leakage Current and Common-Mode EMI Reduction. *IEEE Trans. Power Electron.* **2019**, *34*, 5606–5619. [CrossRef]
4. Spadacini, G.; Grassi, F.; Pignari, S.A. Conducted emissions in the powertrain of electric vehicles. In Proceedings of the 2017 IEEE International Symposium on Electromagnetic Compatibility & Signal/Power Integrity (EMCSI), Washington, DC, USA, 7–11 August 2017; IEEE: Piscataway, NJ, USA, 2017; Volume 69, pp. 1–28. [CrossRef]
5. Robles, E.; Fernandez, M.; Ibarra, E.; Andreu, J.; Kortabarria, I. Mitigation of common mode voltage issues in electric vehicle drive systems by means of an alternative AC-decoupling power converter topology. *Energies* **2019**, *12*, 3349. [CrossRef]
6. Robles, E.; Fernandez, M.; Andreu, J.; Ibarra, E.; Ugalde, U. Advanced power inverter topologies and modulation techniques for common-mode voltage elimination in electric motor drive systems. *Renew. Sustain. Energy Rev.* **2021**, *140*, 110746. [CrossRef]
7. Zhang, J.; Shen, M.; Zhao, X. Study on the Effect of Inverter Modulation Methods and Operating Condition on Common Mode EMI for Motor Drive System; SAE Technical Papers; SAE: Warrendale, PA, USA, 2017; Volume 2017-March. [CrossRef]
8. Vostrov, K.; Pyrhonen, J.; Niemela, M.; Ahola, J.; Lindh, P. Mitigating Noncirculating Bearing Currents by a Correct Stator Magnetic Circuit and Winding Design. *IEEE Trans. Ind. Electron.* **2021**, *68*, 3805–3812. [CrossRef]
9. Weber, T. EMC filters in high voltage traction drive systems. In Proceedings of the IEEE International Symposium on Electromagnetic Compatibility, Hamburg, Germany, 8–12 September 2008. [CrossRef]
10. Zare, F. Practical approach to model electric motors for electromagnetic interference and shaft voltage analysis. *IET Electr. Power Appl.* **2010**, *4*, 727–738. [CrossRef]
11. Schinkel, M.; Weber, S.; Guttowski, S.; John, W.; Reichl, H. Efficient HF Modeling and Model Parameterization of Induction Machines for Time and Frequency Domain Simulations. In Proceedings of the Twenty-First Annual IEEE Applied Power Electronics Conference and Exposition, 2006. APEC '06, Dallas, TX, USA, 19–23 March 2006; IEEE: Piscataway, NJ, USA, 2006; Volume 2006; pp. 1181–1186. [CrossRef]

12. Almandoz, G.; Zarate, S.; Egea, A.; Moreno, Y.; Urdangarin, A.; Moreno, R. High Frequency Modeling of Electric Drives for Electromagnetic Compatibility Analysis. In Proceedings of the 2020 International Conference on Electrical Machines (ICEM), Gothenburg, Sweden, 23–26 August 2020; IEEE: Piscataway, NJ, USA, 2020; pp. 1129–1135. [CrossRef]

13. Hoffmann, A.; Ponick, B. Statistical Deviation of High-Frequency Lumped Model Parameters for Stator Windings in Three-Phase Electrical Machines. In Proceedings of the 2020 International Symposium on Power Electronics, Electrical Drives, Automation and Motion (SPEEDAM), Sorrento, Italy, 24–26 June 2020; IEEE: Piscataway, NJ, USA, 2020; pp. 85–90. [CrossRef]

14. Xiong, Y.; Li, X.; Li, Y.; Zhao, X. A High-frequency Motor Model Constructed Based on Vector Fitting Method. In Proceedings of the 2019 Joint International Symposium on Electromagnetic Compatibility, Sapporo and Asia-Pacific International Symposium on Electromagnetic Compatibility (EMC Sapporo/APEMC), Sapporo, Japan, 3–7 June 2019; IEEE: Piscataway, NJ, USA, 2019; pp. 191–194. [CrossRef]

15. Rahimi, A.; Kanzi, K. Improved High-Frequency Modeling of PMSM Using 3-D Finite Element Analysis. In Proceedings of the 2019 International Power System Conference (PSC), Tehran, Iran, 9–11 December 2019; IEEE: Piscataway, NJ, USA, 2019; pp. 71–78. [CrossRef]

16. Toulabi, M.S.; Wang, L.; Bieber, L.; Filizadeh, S.; Jatskevich, J. A Universal High-Frequency Induction Machine Model and Characterization Method for Arbitrary Stator Winding Connections. *IEEE Trans. Energy Convers.* **2019**, *34*, 1164–1177. [CrossRef]

17. Kwack, Y.; Kim, H.; Song, C.; Moon, M.; Kim, D.H.; Kim, B.; Kim, E.; Kim, J. EMI modeling method of interior permanent magnet synchronous motor for hybrid electric vehicle drive system considering parasitic and dynamic parameters. In Proceedings of the 2015 Asia-Pacific Symposium on Electromagnetic Compatibility (APEMC), Taipei, Taiwan, 26–29 May 2015; IEEE: Piscataway, NJ, USA, 2015; pp. 78–81. [CrossRef]

18. Ruiz-Sarrio, J.E.; Chauvicourt, F.; Gyselinck, J.; Martis, C. High-Frequency Modelling of Electrical Machine Windings Using Numerical Methods. In Proceedings of the 2021 IEEE International Electric Machines & Drives Conference (IEMDC), Hartford, CT, USA, 17–20 May 2021; IEEE: Piscataway, NJ, USA, 2021; pp. 1–7. [CrossRef]

19. Ruiz-Sarrió, J.E. High-Frequency Modelling of Rotating Electrical Machines. Ph.D. Thesis, Technical University of Cluj-Napoca, Cluj-Napoca, Romania, 2022.

20. Mohammed, O.; Ganu, S.; Abed, N.; Liu, S.; Liu, Z. High frequency PM synchronous motor model determined by FE analysis. *IEEE Trans. Magn.* **2006**, *42*, 1291–1294. [CrossRef]

21. Heidler, B.; Brune, K.; Doppelbauer, M. High-frequency model and parameter identification of electrical machines using numerical simulations. In Proceedings of the 2015 IEEE International Electric Machines & Drives Conference (IEMDC), Coeur d'Alene, ID, USA, 10–13 May 2015; IEEE: Piscataway, NJ, USA, 2015; pp. 1221–1227. [CrossRef]

22. Jaritz, M.; Jaeger, C.; Bucher, M.; Smajic, J.; Vukovic, D.; Blume, S. An Improved Model for Circulating Bearing Currents in Inverter-Fed AC Machines. In Proceedings of the 2019 IEEE International Conference on Industrial Technology (ICIT), Melbourne, VIC, Australia, 13–15 February 2019; IEEE: Piscataway, NJ, USA, 2019; pp. 225–230. [CrossRef]

23. Behrendt, C.N.; Dittmann, J.; Knebusch, B.; Ponick, B. Common-Mode Impedance Prediction of a High Frequency Hairpin Stator Winding Based on FEM and Modified Nodal Analysis. In Proceedings of the 2022 International Symposium on Power Electronics, Electrical Drives, Automation and Motion (SPEEDAM), Sorrento, Italy, 22–24 June 2022; IEEE: Piscataway, NJ, USA, 2022; pp. 20–26. [CrossRef]

24. Jaritz, M.; Stieger, N.; Jaeger, C.; Schneider, M.; Vukovic, D.; Blume, S.; Smajic, J. An Improved Model for the Common Mode Impedance in Inverter-Fed AC Machines. In Proceedings of the 2020 International Conference on Electrical Machines (ICEM), Gothenburg, Sweden, 23–26 August 2020; IEEE: Piscataway, NJ, USA, 2020; pp. 1053–1059. [CrossRef]

25. Ferreira, R.; Ferreira, A. Transient model to study voltage distribution in electrical machine windings considering the rotor. *Electr. Power Syst. Res.* **2021**, *195*, 107155. [CrossRef]

26. Radja, N.; Rachek, M.; Larbi, S.N. Improved RLMC-Circuit HF-Dependent Parameters Using FE-EM Computation Dedicated to Predict Fast Transient Voltage Along Insulated Windings. *IEEE Trans. Electromagn. Compat.* **2019**, *61*, 301–308. [CrossRef]

27. Maki, K.; Funato, H.; Shao, L. Motor modeling for EMC simulation by 3-D electromagnetic field analysis. In Proceedings of the 2009 IEEE International Electric Machines and Drives Conference, Miami, FL, USA, 3–6 May 2009; IEEE: Piscataway, NJ, USA, 2009; pp. 103–108. [CrossRef]

28. Moreno, Y.; Almandoz, G.; Egea, A.; Arribas, B.; Urdangarin, A. Analysis of Permanent Magnet Motors in High Frequency—A Review. *Appl. Sci.* **2021**, *11*, 6334. [CrossRef]

29. Moreno, Y.; Egea, A.; Almandoz, G.; Ugalde, G.; Urdangarin, A.; Moreno, R. High-Frequency Modelling of Windings. In Proceedings of the 2022 International Conference on Electrical Machines (ICEM), Valencia, Spain, 5–8 September 2022; IEEE: Piscataway, NJ, USA, 2022; pp. 1232–1238. [CrossRef]

30. Zhu, S.; Shi, B. Modeling of PWM-Induced Iron Losses with Frequency-Domain Methods and Low-Frequency Parameters. *IEEE Trans. Ind. Electron.* **2022**, *69*, 2402–2413. [CrossRef]

31. Smajic, J.; Bucher, M.; Franz, T.; Cranganu-Cretu, B.; Shoory, A.; Tepper, J. Modeling of Frequency Dependent Parameters in Time Domain High Frequency Transformer Simulations. *Procedia Eng.* **2017**, *202*, 251–263. [CrossRef]

32. Skutt, G.R.; Lee, F.C.; Chen, D.; Kohler, W. High-Frequency Dimensional Effects in Ferrite-Core Magnetic Devices. Ph.D. Thesis, Virginia Polytechnic Institute and State University, Blacksburg, VA, USA, 1996.
33. Abeywickrama, K.G.B.; Daszczynski, T.; Serdyuk, Y.V.; Gubanski, S.M. Determination of complex permeability of silicon steel for use in high-frequency modeling of power transformers. *IEEE Trans. Magn.* **2008**, *44*, 438–444. [CrossRef]